



# Hydrothermal synthesis of MnO<sub>2</sub>/Fe(0) composites from Li-ion battery cathodes for destructing sulfadiazine by photo-Fenton process

Xing Chen<sup>a,b,\*</sup>, Fang Deng<sup>a,b</sup>, Xu Liu<sup>a,b</sup>, Kang-Ping Cui<sup>a</sup>, Rohan Weerasooriya<sup>b,c</sup>

<sup>a</sup> Key Laboratory of Nanominerals and Pollution Control of Higher Education Institutes, School of Resources and Environmental Engineering, Hefei University of Technology, Hefei 230009, PR China

<sup>b</sup> Key Lab of Aerospace Structural Parts Forming Technology and Equipment of Anhui Province, Institute of Industry and Equipment Technology, Hefei University of Technology, Hefei 230009, PR China

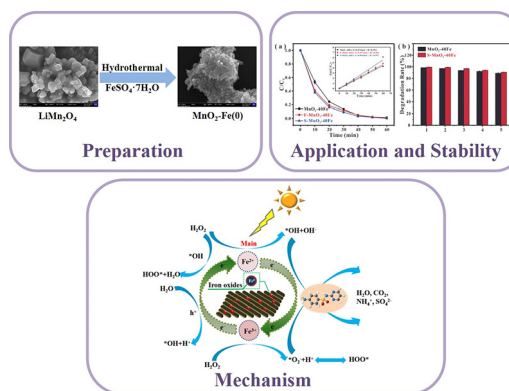
<sup>c</sup> National Centre for Water Quality Research, National Institute of Fundamental Studies Hantana, Kandy, Sri Lanka

## HIGHLIGHTS

- MnO<sub>2</sub>/Fe(0) nanocomposites were synthesized via a hydrothermal method.
- Spent Li-ion battery cathode materials were reclaimed for photo-Fenton catalyst.
- The degradation efficiency increased 5.4 times after loading Fe(0) on the MnO<sub>2</sub>.
- As-prepared MnO<sub>2</sub>/Fe(0) nanocomposites showed good repeatability.
- The possible mechanism and pathway of sulfadiazine degradation were proposed.

## GRAPHICAL ABSTRACT

Hydrothermal conversion of Li-ion battery cathode materials into MnO<sub>2</sub>/Fe(0) composites: synthesis and its environmental application.



## ARTICLE INFO

### Article history:

Received 11 December 2020

Received in revised form 22 January 2021

Accepted 6 February 2021

Available online 11 February 2021

Editor: Yifeng Zhang

### Keywords:

Sulfadiazine

Li-ion battery cathode material

MnO<sub>2</sub>

Nano zero-valent iron

Photo-Fenton

## ABSTRACT

Harmless treatment of antibiotics, and recovery of precious metals from the spent Li-ion battery are two typical environmental issues with rapid development of the society. Presently, we reclaimed Mn from the spent Li-ion battery cathode materials for hydrothermally synthesizing MnO<sub>2</sub>/Fe(0) composites, which were used as the efficient heterogeneous photo-Fenton catalyst. The new composite was well characterized by X-ray diffractometer (XRD), scanning electron microscope (SEM), high resolution transmission electron microscopy (HRTEM), X-ray photoelectron spectroscopy (XPS), photoluminescence (PL) and Brunauer-Emmett-Teller (BET) methods before optimizing their usage for sulfadiazine destruction. The catalytic efficiency of the MnO<sub>2</sub> substrate was enhanced by impregnating different proportions of Fe(0) into the substrate. The MnO<sub>2</sub>: Fe(0) molar ratio at 40:1 (MnO<sub>2</sub>-40Fe) shows optimal catalytic activity. Sulfadiazine degradation by 0.2 g/L MnO<sub>2</sub>-40Fe, 6 mM H<sub>2</sub>O<sub>2</sub> in pH 3 is almost 98.6%, and it follows first-order kinetics. The MnO<sub>2</sub> and nano zero-valent iron synthesized using spent cathode of Li-ion batteries is equally efficient in sulfadiazine even after five times repeated use. As elucidated by mass spectroscopic data, sulfadiazine degradation by MnO<sub>2</sub>-40Fe was a multi-faceted photo-Fenton process which results in CO<sub>2</sub>, H<sub>2</sub>O, NH<sub>4</sub><sup>+</sup> and SO<sub>4</sub><sup>2-</sup> as final products. The excellent degradation performance of the as-prepared catalyst might be attributed to the introduction of nano zero-valent iron on the

\* Corresponding author at: Key Laboratory of Nanominerals and Pollution Control of Higher Education Institutes, School of Resources and Environmental Engineering, Hefei University of Technology, Hefei 230009, PR China.

E-mail address: [xingchen@hfut.edu.cn](mailto:xingchen@hfut.edu.cn) (X. Chen).

nanostructured MnO<sub>2</sub>, which not only provides more active sites, but also has a synergistic effect with MnO<sub>2</sub> and light irradiation, leading to the generation of large amounts of activated radicals for destructing sulfadiazine. This work provides a promising method for reclamation of spent Li-ion battery cathode for environmental applications.

© 2021 Elsevier B.V. All rights reserved.

## 1. Introduction

Antibiotics are widely used throughout the world to treat infectious diseases, and they enter soils and water systems through leachates of sewage, manure and pharmaceutical wastes (Baquero et al., 2008; Kümmerer, 2004; Liu et al., 2018b; Thiele-Bruhn and Aust, 2004). They are persistent in the environment, and maintain toxicity to the hematopoietic system, posing a serious threat to the environment and humans (Li et al., 2020a). Sulfadiazine, a member of the sulfonamides class, is extensively used in agriculture and has low retention capacity in soils that results in their ubiquity in water (Chang et al., 2008; Michael et al., 2013; Neafsey et al., 2010). Conventional water treatment methods do not design to degrade recalcitrant antibiotics fully (Patel et al., 2019). However, advanced water treatment methods such as photolysis, oxidation, membrane filtration and adsorption are used to remediate pharmaceutical products with some success. Both membrane and adsorption methods do not destruct organic pollutants but merely concentrate in a limited volume. Although oxidation and photolysis methods degrade pharmaceuticals, they often render intermediates that may be perhaps more toxic than parent compounds (Liu et al., 2019; Patel et al., 2019). Photo-Fenton technology converts organic pollutants to CO<sub>2</sub> and H<sub>2</sub>O using hydroxyl (\*OH) and superoxide radicals (\*O<sub>2</sub><sup>-</sup>). Photo-Fenton technology methods are particularly attractive due to its non-selective destruction of organic pollutants, efficiency, easy operation and low cost (Zhang et al., 2019). The photo-Fenton processes are classified as homogeneous and heterogeneous. In heterogeneous photo-Fenton processes, the separation of the catalyst from the treated solution does not require laborious efforts and potential reusability of the catalyst is feasible (Gomes et al., 2017).

And at the same time, the accumulation of spent Li-ion batteries is a serious environmental issue that requires urgent attention. For example, from the usage rate of electric cars alone in 2017, over 250,000 tons of waste batteries are expected by the end of their lives (Harper et al., 2019). Extraction of precious metals from spent Li-ion batteries is not always feasible due to complicated extraction protocols, secondary pollution threats, and high extraction costs involved (Gao et al., 2017; Yang et al., 2016). Lin et al. (2019) reported a modified sulfation roasting method to eliminate the serious gas emission with improving the atomic efficiency of sulfuric acid. The cathode of the lithium manganate batteries commonly used manganese. For recovery of Mn from the spent cathode materials, the Mn<sup>2+</sup> ions in the leaching solution could be oxidized by some strong oxidants, such as KMnO<sub>4</sub> (Wang et al., 2009), or NaClO (Barik et al., 2017), etc. resulting in MnO<sub>2</sub> form for separation. Hydrothermal treatment might be one of the promising routes for reclamation of the spent Mn-contained cathode materials of lithium batteries, which can be used as the starting precursor for the fabrication of MnO<sub>2</sub> based photo-Fenton catalyst for pollution control (Harper et al., 2019; Qu et al., 2011).

Previously, MnO<sub>2</sub> as an environmentally friendly material, is widely used to mitigate organic toxicants. The MnO<sub>2</sub> based catalysts have high specific surface area & adsorption capacity, and they are environmentally benign. The catalyst efficiency can be improved when MnO<sub>2</sub> is incorporated with the transition metals or metal oxides. Wang et al. (2018b) obtained MnO<sub>2</sub> from the cathode of the spent lithium battery through a simple washing and recycling process and used it to activate PMS to degrade the pollutants. Zhao

et al. (2018) prepared a novel spherical Fe<sub>3</sub>O<sub>4</sub>/γ-MnO<sub>2</sub> with magnetic properties, which has an adequate adsorption capacity to remove fluoride in water. Gheju and Balcu (2019) found that MnO<sub>2</sub> and Fe(0) composite has a good Cr(VI) removal efficiency because MnO<sub>2</sub> promoted Fe(0) oxidative dissolution. Ploychompoo et al. (2020) fabricated MIL-100(Fe)/rGO/δ-MnO<sub>2</sub> with excellent adsorptive removal of both As(III) and As(V). Habibi and Mosavi (2017) studied MnO<sub>2</sub>/Fe<sub>2</sub>O<sub>3</sub> composite for photocatalytic degradation of cresol fast violet dye in solution. These results tempted us to fabricate MnO<sub>2</sub> and Fe(0) composite material for photo-Fenton degradation of recalcitrant antibiotics.

We synthesized MnO<sub>2</sub> and nano zero-valent iron composites via a one-step simple hydrothermal method. The composites were characterized by XRD, SEM, HRTEM, XPS, PL and BET methods. MnO<sub>2</sub>-Fe(0) with a small amount of iron leaching was used to photo-Fenton degrade sulfadiazine. The as-prepared composites were used for photo-Fenton degradation of sulfadiazine with a small amount of iron leaching, and the Fe(0) contents were varied to yield optimal oxidation efficiency. Loading zero-valent iron effectively improved the catalytic ability of MnO<sub>2</sub>. After that, the experimental parameters such as pH, H<sub>2</sub>O<sub>2</sub> concentration and catalyst dosage, were also varied for sulfadiazine removal. The spent cathode material of Li-ion batteries was used as a starting material for fabrication of MnO<sub>2</sub> and Fe(0) composites. The recycling efficiency of the catalyst was also examined using sulfadiazine degradation. It shows that our research uses one solid waste to treat another wastewater, reclaiming the spent cathode material of Li-ion batteries.

## 2. Materials and methods

### 2.1. Chemicals and reagents

Sulfadiazine (C<sub>10</sub>H<sub>10</sub>N<sub>4</sub>O<sub>2</sub>S, 99% purity), lithium manganate (LiMn<sub>2</sub>O<sub>4</sub>), ferrous sulfate heptahydrate (FeSO<sub>4</sub>·7H<sub>2</sub>O), sulfuric acid (H<sub>2</sub>SO<sub>4</sub>), sodium hydroxide (NaOH), hydrogen peroxide (H<sub>2</sub>O<sub>2</sub>), hydrochloric acid (HCl), hydroxylamine hydrochloride (HONH<sub>2</sub>Cl), glacial acetic acid (C<sub>2</sub>H<sub>4</sub>O<sub>2</sub>), ammonium acetate (CH<sub>3</sub>COONH<sub>4</sub>), phenanthroline (C<sub>12</sub>H<sub>8</sub>N<sub>2</sub>·H<sub>2</sub>O), ammonium ferrous sulfate ((NH<sub>4</sub>)<sub>2</sub>Fe(SO<sub>4</sub>)<sub>2</sub>·6H<sub>2</sub>O), tert-butyl alcohol (C<sub>4</sub>H<sub>10</sub>O), benzoquinone (C<sub>6</sub>H<sub>4</sub>O<sub>2</sub>), silver nitrate (AgNO<sub>3</sub>), ethylenediaminetetraacetic acid (C<sub>10</sub>H<sub>16</sub>N<sub>2</sub>O<sub>8</sub>), titanium potassium oxalate (K<sub>2</sub>TiO(C<sub>2</sub>O<sub>4</sub>)<sub>2</sub>), 5,5-dimethyl-1-pyrrolone N-oxide (C<sub>6</sub>H<sub>11</sub>NO, DMPO) were purchased from Sigma-Aldrich (USA). All chemical reagents used in this work were analytical reagent grade.

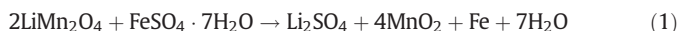
The cathode materials of spent Li-ion batteries were collected from the Li-ion batteries after recycled for 100 times from Anhui Li Tian-Xia Electronic Technology Co. Ltd.

### 2.2. Preparation of catalyst

A hydrothermal method was used to prepare MnO<sub>2</sub>, and MnO<sub>2</sub> loaded nano zero-valent iron composites. Initially, 1.36 g LiMn<sub>2</sub>O<sub>4</sub> I and 10 mL 1 M H<sub>2</sub>SO<sub>4</sub> solution were mixed, and transferred to a 50 mL Teflon stainless steel reactor, and heated at 140 °C for 24 h. The substrate was then cooled to room temperature, and washed with deionized water followed by C<sub>2</sub>H<sub>5</sub>OH until the pH of the leachates changed to pH 7. The resulted black paste was dried at 100 °C in an oven

overnight and then cooled dried residue was ground with an agate mortar to pass through the 200 mesh sieves.

The synthesis method of MnO<sub>2</sub> loaded nano zero-valent iron composite is essentially same as with the MnO<sub>2</sub> except the variations shown below: 1.36 g LiMn<sub>2</sub>O<sub>4</sub>, 10 mL 1 M H<sub>2</sub>SO<sub>4</sub> and pre-determined amounts of FeSO<sub>4</sub>·7H<sub>2</sub>O were well mixed in a 50 mL Teflon coated stainless steel reactor. The molar ratios of Mn: Fe were 20:1 (hereafter MnO<sub>2</sub>-20Fe), 40:1 (MnO<sub>2</sub>-40Fe), 60:1 (MnO<sub>2</sub>-60Fe) and 80:1 (MnO<sub>2</sub>-80Fe). The rest of the steps was given as in MnO<sub>2</sub> synthesis process. The following reaction can summarize the entire process of MnO<sub>2</sub>-Fe composites:



### 2.3. Materials characterization

X-ray diffractometer (PANalytical X'Pert Pro, Netherlands) was used to analyze the crystalline structure of the MnO<sub>2</sub> and MnO<sub>2</sub>-Fe composites using 5° to 70° of 2θ scan range (40 kV and 30 mA applied current). The morphology of the surface structures of the composites was observed by a cold field emission scanning electron microscope (SEM; Hitachi, Japan), JEM-1400F transmission electron microscopy (TEM; JEOL, Japan) and JEM-2100F transmission electron microscopy (HRTEM; JEOL, Japan). A small amount of the composite was dissolved evenly in ethanol, and then spread covering the surface of silica wafer or the copper mesh before microimaging. X-ray photoelectron spectroscopy (XPS; Shimadzu, Japan) was used to determine the atomic composition and valence states of Mn, Fe and O of the composites. All XPS data analyses were carried out dedicated code (PeakFit V4.12). The specific surface area and the pore size distribution of the composites was also determined by brunauer emmett teller analyzer (Autosorb-IQ3, Quantachrome, USA). The UV-vis diffuse reflectance spectroscopy (DRS) was researched on UV-vis near-infrared spectrophotometer (Cary-5000, Agilent, USA), using BaSO<sub>4</sub> as reference substance. The photoluminescence (PL) spectra of the composites were obtained by steady-state/lifetime spectrofluorometer (Fluorolog-3-Tau, Horiba, Japan). Photocurrent response was measured by a three-electrode electrochemical system.

### 2.4. Determination of photo-Fenton activity

In a typical experiment, 50 mL sulfadiazine, 10 mg MnO<sub>2</sub> or MnO<sub>2</sub>-Fe was added to a photochemical reactor. All pH adjustments were made either with 0.1 M NaOH or 0.1 M HCl. The sulfadiazine and MnO<sub>2</sub>-Fe suspensions were then equilibrated under dark for 40 min at 500 r/min. Before the photo-radiation, the initial sulfadiazine (C<sub>0</sub>) concentration was determined. Then the reactor was exposed to photo radiation (500 W Xe lamp, XPA-7; Xujiang Electromechanical Plant, China), and sample aliquots were taken at regular intervals. The samples were centrifuged for 5 min and filtered through 0.22 μm, and the residual sulfadiazine concentration was determined by colorimetry.

### 2.5. Analytical methods

A colorimetric method was adapted for the determination of H<sub>2</sub>O<sub>2</sub> concentration by UV visible method at 385 nm using titanium potassium oxalate as a color-developing agent (Sellers, 1980). While sulfadiazine concentration was measured in the same way at the wavelength of 265 nm (Zhang et al., 2007). The total organic carbon (TOC) in the samples was determined by TOC/TN analyzer (Multi N/C 3100). The pH measurements were carried out with a pH Meter (HACHHQ30d, USA). The presence of \*OH and \*O<sub>2</sub><sup>-</sup> radicals in the solution was determined by electron paramagnetic resonance spectrometer after capturing them with DMPO (EPR/ESR JEOL, JES-FA 200, Japan). Fe<sup>2+</sup> and Fe<sup>3+</sup> concentrations were measured using a spectrophotometer

by phenanthroline method (To et al., 1999). Used 50 mM and 100 mM DMPO to capture \*OH and \*O<sub>2</sub><sup>-</sup> free radicals, and tested their presence by electron paramagnetic resonance spectrometer. Tert-butyl alcohol (TBA), benzoquinone (BQ), AgNO<sub>3</sub> and EDTA were used to quench \*OH, superoxide (\*O<sub>2</sub><sup>-</sup>), electrons (e<sup>-</sup>) and holes (h<sup>+</sup>) before sulfadiazine detection. During the degradation process the intermediate products of sulfadiazine were determined by high-performance liquid chromatography-mass spectrometry (HPLC-MS; Agilent 1290/6460, USA). The relative toxicities of the intermediate products of sulfadiazine were simulated with a toxicity estimation software tool (T.E.S.T, USA).

## 3. Results and discussion

### 3.1. X-ray diffraction of MnO<sub>2</sub> and MnO<sub>2</sub>-Fe composites

XRD spectral data shown in Fig. 1 were used to determine the crystallinity of MnO<sub>2</sub> and MnO<sub>2</sub>-Fe composites. The X-ray diffraction peaks at 28.66, 37.36, 40.92, 42.78, 46.02, 56.66, 59.30, 64.92 and 67.18° respectively correspond to (110), (101), (200), (111), (210), (211), (220), (002) and (310) planes of MnO<sub>2</sub> which further confirms the solid phase as β-MnO<sub>2</sub> (reference data MnO<sub>2</sub>, JCPDS PDF#81-2261). Additionally, in MnO<sub>2</sub>-Fe composites, the peak at 65.14° corresponds to (200) metallic iron plane (JCPDS PDF#87-0722). With the increase of iron content, the XRD patterns of MnO<sub>2</sub>-Fe(0) change. The characteristic peaks of MnO<sub>2</sub> shift to decreased 2θ values, which may be related to the expansion of the MnO<sub>2</sub> lattice (Wang et al., 2018b). The characteristic peak of γ-MnO<sub>2</sub> appears in MnO<sub>2</sub>-Fe(0), and 38.43° corresponds to (230) plane of γ-MnO<sub>2</sub> (JCPDS PDF#14-0644). As a whole, the presence of sharp X-ray peaks confirms well crystalline materials.

The microstructures and surface morphology of MnO<sub>2</sub> and MnO<sub>2</sub>-Fe composites were determined by electron microscopic measurements (Fig. S1). In MnO<sub>2</sub>-80Fe, only a few surface sites are loaded with Fe(0). When compared the SEM images of MnO<sub>2</sub>-Fe composites, the MnO<sub>2</sub>-40Fe sample showed optimal crystallinity (Fig. S1c). Therefore, this sample was used for a detailed analysis, as shown in Fig. 2b-e. MnO<sub>2</sub>-40Fe after the reaction was characterized (Fig. S1d), and its microstructure didn't change significantly. The TEM data show nanorods in MnO<sub>2</sub>-40Fe (Fig. 2a). The thickness of MnO<sub>2</sub> nanorods increases with the Fe(0) loading from 75 nm (MnO<sub>2</sub>) to 120 nm (MnO<sub>2</sub>-40Fe). The details of thickness variations of the nanorods with the Fe(0) loading are shown in Fig. S2. HRTEM image of MnO<sub>2</sub>-40Fe is shown in

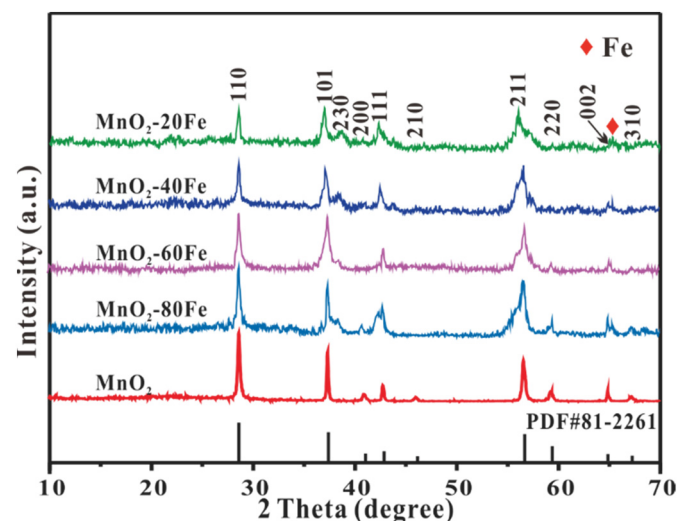


Fig. 1. XRD of MnO<sub>2</sub> and MnO<sub>2</sub>-Fe composites.

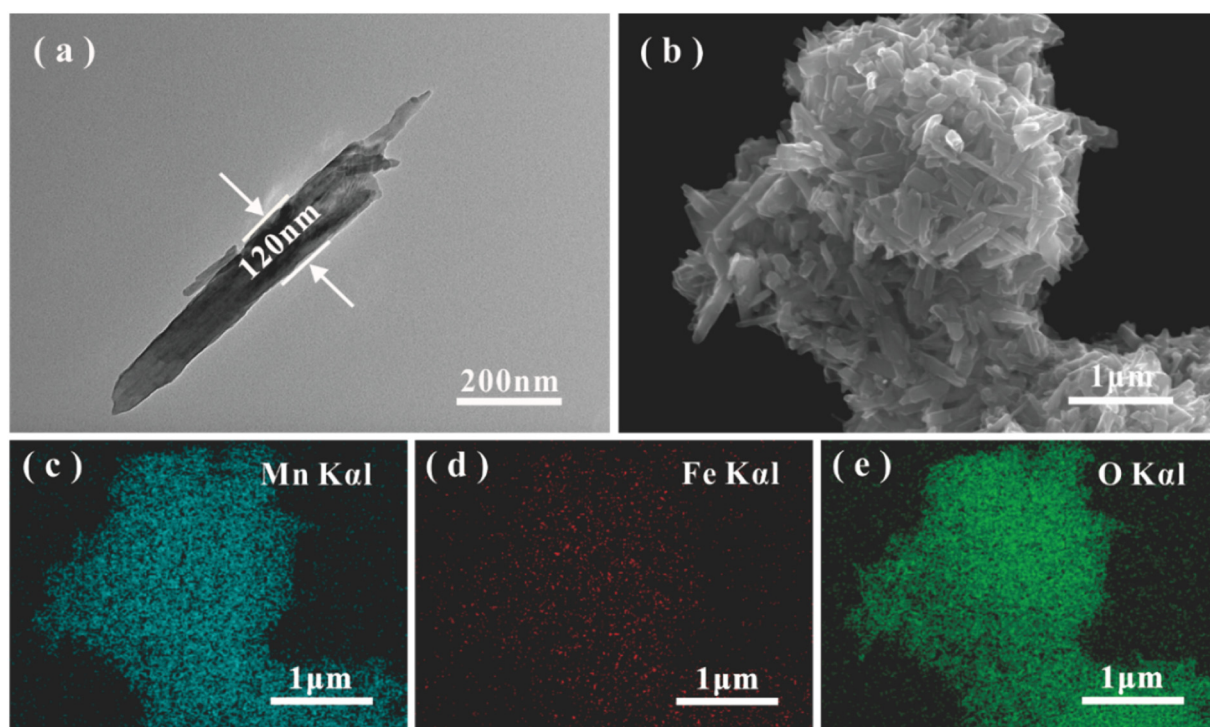


Fig. 2. TEM (a), SEM image (b) and elemental mapping images (c-e) of MnO<sub>2</sub>-40Fe.

Fig. S3b. The element mapping diagrams (Fig. S3c-f) confirm that three elements of Mn, Fe and O are evenly distributed. EDS analysis further confirms the existence of Mn, Fe and O in MnO<sub>2</sub>-40Fe, and the mass ratio of iron is 1.38%.

### 3.2. Effect of experimental conditions on the degradation of sulfadiazine

Different operating factors such as catalyst's Fe(0) content, substrate loading, H<sub>2</sub>O<sub>2</sub> concentration, and solution pH were taken as main variables to examine the efficiency of sulfadiazine photo degradation. The following conditions were used in a typical experiment; 20 mg/L sulfadiazine, 6 mM H<sub>2</sub>O<sub>2</sub>, 0.20 g/L catalyst, and pH 3. A given parameter was optimized at a time while fixing others in specific values. The degradation efficiencies of sulfadiazine by MnO<sub>2</sub>-Fe composites are superior compared to bare MnO<sub>2</sub>. As shown in Fig. 3a, within 60 min of reaction time, the sulfadiazine degradation efficiencies by MnO<sub>2</sub>-20Fe, MnO<sub>2</sub>-40Fe, MnO<sub>2</sub>-60Fe, MnO<sub>2</sub>-80Fe and MnO<sub>2</sub> are 98.8%, 98.6%, 95.8%, 94.7% and 15.4% respectively. The removal of sulfadiazine reaches 30.8% by pure zero-valent iron. The presence of Fe(0) in the composites enhances the sulfadiazine degradation by Fenton-like oxidation (Xu and Wang, 2011). The role of MnO<sub>2</sub> in the catalyst seems to enhance the electron shuttling among substrates in the production of \*OH radicals. Both the MnO<sub>2</sub>-40Fe and MnO<sub>2</sub>-20Fe composites show comparable efficiency for sulfadiazine degradation. We selected MnO<sub>2</sub>-40Fe for subsequent investigations due to its low loading of Fe(0).

The effect of substrate loading on the degradation efficiency of MnO<sub>2</sub>-40Fe was examined by varying sulfadiazine concentration, and the results are shown in Fig. 3b. The degradation efficiency increased at low sulfadiazine concentrations. As sulfadiazine concentration is increased the degradation efficiency is decreased due to limited availability of catalytic sites.

As shown in Fig. 3c, the effect of MnO<sub>2</sub>-40Fe dosage on the degradation of sulfadiazine was examined. The sulfadiazine degradation has steadily increased from 74.0% to 98.6% with 60 min with the catalyst content. However, at excess catalyst loading, a decline in the sulfadiazine degradation is observed. The aggregation of catalysts may reduce

its activity. Therefore, maintaining the concentration of the catalyst at an optimal value is vital for efficient sulfadiazine degradation.

The pH exerts an effect on the performance of catalyst and oxidizing capacity of the materials (Liu et al., 2018c; Tang and Wang, 2018; Xu and Wang, 2011). The role of pH is significant in degrading sulfadiazine by MnO<sub>2</sub>-40Fe since it affects the production of \*OH production by Fenton like mechanisms as shown elsewhere (Pignatello et al., 2006). The photo-Fenton effect of MnO<sub>2</sub>-40Fe on sulfadiazine degradation has significantly affected by the solution pH (Fig. 3d). When the solution pH increases from 2 to 3, the sulfadiazine degradation efficiency has nearly doubled within 60 min. At acidic pH, the \*OH radicals can scavenge by H<sup>+</sup> (Bai et al., 2017; Liu et al., 2018a), and the corrosion rate of the catalyst is also increased. Both of the processes showed a decline of degradation of sulfadiazine at extreme acidic conditions. Interestingly when pH is increased from 3 to 7, the efficiency of sulfadiazine degradation has reduced from 98.6% to 24.7%. When pH > 3, both Fe<sup>2+</sup> and Fe<sup>3+</sup> are liable to form iron oxides/ hydroxides which induce surface passivation that limits catalytic sites for sulfadiazine degradation (Bai et al., 2017; Liu et al., 2018a). Another reason why the degradation rate decreases with the increase of pH is due to the lowering redox potential of hydroxyl radicals (\*OH + e<sup>-</sup> + H<sup>+</sup> = H<sub>2</sub>O, E<sup>h</sup> = 2.73 V) and spontaneous decomposition of H<sub>2</sub>O<sub>2</sub> (H<sub>2</sub>O<sub>2</sub> + e<sup>-</sup> + H<sup>+</sup> = \*OH + H<sub>2</sub>O, E<sup>h</sup> = 0.80 V) (Liu et al., 2018c; Xu and Wang, 2011). The MnO<sub>2</sub>-40Fe has the highest degradation efficiency of sulfadiazine at pH 3.

Fig. 3e illustrates the effect of the H<sub>2</sub>O<sub>2</sub> addition on the degradation efficiency of sulfadiazine by MnO<sub>2</sub>-40Fe. When the H<sub>2</sub>O<sub>2</sub> concentration increased from 4 to 6 mM, the degradation rates only slightly increased (e.g. 4 mM H<sub>2</sub>O<sub>2</sub> 97.7% and 6 mM H<sub>2</sub>O<sub>2</sub> 98.6%). With the increasing H<sub>2</sub>O<sub>2</sub> concentration, the removal of sulfadiazine solution also increased, but this effect is not apparent from the data shown. From an economic perspective, we used 6 mM H<sub>2</sub>O<sub>2</sub> to remove sulfadiazine.

To further explain the importance of light and H<sub>2</sub>O<sub>2</sub> on MnO<sub>2</sub>-40Fe catalysis, additional experiments were performed, and the results are shown in Fig. 3f. In the dark, the degradation efficiency of sulfadiazine by MnO<sub>2</sub>-40Fe was only 3.1% due to low production of \*OH by H<sub>2</sub>O<sub>2</sub> (Li et al., 2020a). The sulfadiazine removal rate of single hydrogen

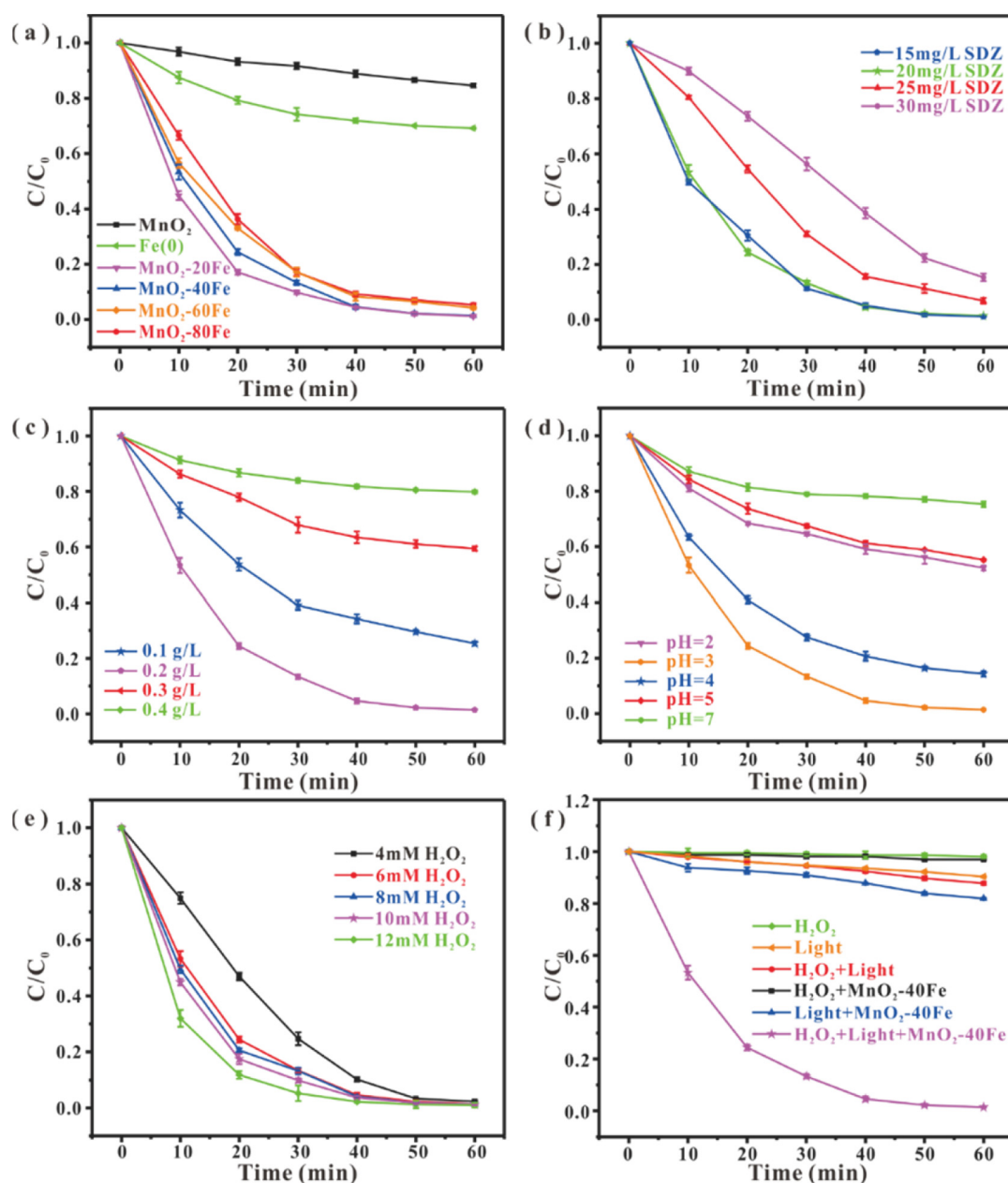


**Fig. 3.** The effect of operating factors on degrading SDZ by the photo-Fenton reaction system: Iron content in catalysts (a); the initial concentration of SDZ (b); the addition amount of  $\text{MnO}_2\text{-40Fe}$  (c); pH (d);  $\text{H}_2\text{O}_2$  concentration (e); the different reaction systems (f). Except for the parameters studied, other parameters:  $[\text{SDZ}]_0 = 20 \text{ mg/L}$ ,  $[\text{H}_2\text{O}_2]_0 = 6 \text{ mM}$ ,  $[\text{Catalyst}]_0 = 0.2 \text{ g/L}$ ,  $[\text{pH}]_0 = 3$ ,  $T = 20^\circ \text{C}$  and 500 W xenon lamp.

peroxide or light was 2% and 9.7%, respectively. In the presence of light, the electron and holes generation were enhanced, which accelerated activation of  $\text{H}_2\text{O}_2$  for  $\cdot\text{OH}$  production. Similarly, when a catalyst is not used, either in the presence or absence of photons, the production of free radicals is not efficient; therefore, the degradation of sulfadiazine was only 18.1%. When the light,  $\text{MnO}_2\text{-40Fe}$  catalyst and  $\text{H}_2\text{O}_2$  are present, the degradation efficiency is greatly improved due to the efficient production of  $\cdot\text{OH}$  radicals.

### 3.3. The mineralization rate of sulfadiazine and the utilization rate of $\text{H}_2\text{O}_2$ in $\text{MnO}_2\text{-40Fe}/\text{H}_2\text{O}_2/\text{light}$ system

The degradation of sulfadiazine by  $\text{MnO}_2\text{-40Fe}$  was evaluated by monitoring aqueous TOC content to develop an empirical degradation model. The optimized experimental conditions shown in Section 3.2

are used for the experimental setup. The TOC includes the residual sulfadiazine and its intermediates. The TOC content in solution rapidly declines with the time showing the fastest kinetics within the first 10 min (Fig. S4), which is ascribed to sulfadiazine degradation. As shown in Fig. S5, almost 75.1%  $\text{H}_2\text{O}_2$  is utilized within 10 min. Which implies that 6 mM  $\text{H}_2\text{O}_2$  is nearly exhausted by the catalyst to yield free radicals which result in 69.6% TOC reduction.

### 3.4. Comparison of synthesized $\text{MnO}_2$ and $\text{MnO}_2\text{-40Fe}$

The XPS, CV, EIS, BET and DRS measurements were made to identify the properties of the  $\text{MnO}_2\text{-40Fe}$  catalyst. In XPS, we used the spectral peaks of Fe 2p (Fig. S6b), Mn 2p (Fig. S6c), O 1s (Fig. S6d) and the wide-scan spectrum to analyze the surface structure of  $\text{MnO}_2\text{-40Fe}$  before and after the reaction. As shown in Fig. S6a, we noted that

MnO<sub>2</sub>-40Fe is mainly composed of O, Mn and Fe, and their atomic compositions are 68.79%, 26.88% and 4.33%, respectively. The characteristic peak of Fe 2p has six components: Fe<sup>0</sup> (Fe 2p<sub>1/2</sub>: 706.6 eV), Fe<sup>2+</sup> (Fe 2p<sub>1/2</sub>: 709.8 eV), Fe<sup>3+</sup> (Fe 2p<sub>3/2</sub>: 710.8 eV and 713.9 eV; Fe 2p<sub>1/2</sub>: 724.6 eV), and the satellite Fe 2p peak (Fe 2p<sub>1/2</sub>: 718.3 eV) (Dickinson and Scott, 2010; Xu and Wang, 2017; Yan et al., 2010). The presence of Fe<sup>2+</sup> and Fe<sup>3+</sup> peaks on the MnO<sub>2</sub>-40Fe catalyst indicate inevitable oxidation of the outer surface of nano zero-valent iron with iron oxide during its preparation (Yan et al., 2010). The peak of 718.3 eV disappears in the used MnO<sub>2</sub>-40Fe, but two new binding energies at 717.1 eV and 719 eV are Fe 2p<sub>3/2</sub> and the satellite peak, respectively. That reflects the presence of Fe<sub>2</sub>O<sub>3</sub> (Hao et al., 2017; Song et al., 2017). The peak intensity of 713.9 eV is reduced. This may be related to the cycle Fe<sup>2+</sup> and Fe<sup>3+</sup> in MnO<sub>2</sub>-40Fe/H<sub>2</sub>O<sub>2</sub>/light system. Besides, the binding energy peaks at 642.5 eV and 654.1 eV are traced to the contributions of Mn 2p<sub>3/2</sub> and Mn 2p<sub>1/2</sub>, and it also reveals that manganese in the catalyst is in Mn<sup>4+</sup> state (Hao et al., 2017; Wang et al., 2018a). Mn 2p<sub>3/2</sub> and Mn 2p<sub>1/2</sub> are divided into four peaks of 642.5 eV, 645.6 eV, 654.1 eV and 656.5 eV, indicating the production of Mn<sup>3+</sup> (Ploychompoo et al., 2020). These results suggest that Fe<sup>2+</sup> is oxidized to Fe<sup>3+</sup> along with the reduction of Mn<sup>4+</sup> to Mn<sup>3+</sup> (Lyu et al., 2019). The O 1s has two peaks from Fig. S6d, namely 529.7 eV and 531.3 eV, which represent metal oxide (M-O) and surface adsorbed oxygen (O<sub>ads</sub>), respectively (Lyu et al., 2019). The spectral peaks of O 1s for the used MnO<sub>2</sub>-40Fe are unchanged.

Fig. S7a show the continuous CV scan of MnO<sub>2</sub> and MnO<sub>2</sub>-40Fe. The CV curves indicate the electron transferability of a substance (Kennedy and Joel, 2006). The glassy carbon electrode modified with MnO<sub>2</sub> or MnO<sub>2</sub>-40Fe was placed in K<sub>3</sub>[Fe (CN)<sub>6</sub>] solution to study the cyclic voltammetry behavior. The result shows that the reduction potential ( $\Delta E_p$ ) of MnO<sub>2</sub>-40Fe (0.268 V) is 1.35 times greater than that of MnO<sub>2</sub> (0.198 V), indicating that MnO<sub>2</sub>-40Fe has better redox properties than MnO<sub>2</sub>. To explore the electron transport properties of the catalyst, we performed electrochemical impedance spectroscopy (EIS) experiments, as shown in Fig. S7b. Theoretically, the diameter of the semicircle represents the strength of the polarization resistance (Ruiz-Camacho et al., 2017), and increasing the electrode potential makes the diameter of the semicircle larger, which implies that the charge transfer resistance augments (Singh et al., 2015). The semicircle diameter of MnO<sub>2</sub>-40Fe is smaller than MnO<sub>2</sub>, indicating that the polarization resistance of former is low; hence the electron transfer rate of the MnO<sub>2</sub>-40Fe modified GCE is faster.

The photophysical behavior of MnO<sub>2</sub> and MnO<sub>2</sub>-40Fe was investigated by steady-state/lifetime spectrofluorometer, the result was shown in Fig. S7c. Under the excitation of 370 nm wavelength, photoluminescence spectrum of MnO<sub>2</sub> has a broad peak at 465 nm. The higher PL intensity means the greater recombination rate of electrons and holes. MnO<sub>2</sub>-40Fe shows the lower PL intensity than MnO<sub>2</sub>, indicating that zero-valent iron loading on MnO<sub>2</sub> can effectively improve the transference ability of photo-generated charge carrier. In order to further study the charge carrier separation of MnO<sub>2</sub> and MnO<sub>2</sub>-40Fe, we conducted the transient photocurrent experiments, as shown in Fig. S7d. The photocurrent of MnO<sub>2</sub>-40Fe is stronger than MnO<sub>2</sub>, suggesting that zero-valent iron promotes the separation of charge carrier and reduces the recombination rate of electrons and holes.

The nitrogen adsorption-desorption isotherms of MnO<sub>2</sub> and MnO<sub>2</sub>-40Fe is shown in Fig. S7e, which are the typical III genre with H<sub>3</sub>-genre hysteresis loop (Hadi and Hajar, 2021). As the pressure ratio (P/P<sub>0</sub>) increases, the adsorption capacity of MnO<sub>2</sub>-40Fe is slightly higher than MnO<sub>2</sub>. After Fe(0) loading onto MnO<sub>2</sub>, the average pore diameter increases from 76.71 nm to 118.95 nm, which is consistent with the TEM data. With increasing iron, the surface of MnO<sub>2</sub> is decorated by nano zero-valent iron, which leads to an increase in the average pore diameter of MnO<sub>2</sub>-40Fe (Xiang et al., 2019). However, the specific surface area of the MnO<sub>2</sub> and MnO<sub>2</sub>-40Fe decreases from 32.43 to 27.61 m<sup>2</sup>/g,

respectively. This is because zero-valent iron loading on MnO<sub>2</sub> results in changing the specific surface area. However, as the iron content increases, the reactive sites also increase, which has a significant effect on the activity of the catalyst (Li et al., 2020b). Therefore, a larger surface area of the catalyst is conducive to have full access to other substances, thereby improving its catalytic activity (Chen et al., 2019a).

UV-vis diffuse reflectance spectra were used to investigate the optical property of MnO<sub>2</sub> and MnO<sub>2</sub>-40Fe, and the result was shown in Fig. S8a. MnO<sub>2</sub> exhibits the strong absorption intensity in the entire UV-vis light field, which is attributed to its excellent photoelectric properties (Wang et al., 2017). Nano zero-valent iron does not significantly change the absorbance of MnO<sub>2</sub>. In addition, the band gaps of catalysts could be obtained by the equation:  $E_g = 1240/\lambda$  ( $\lambda$  is the wavelength) (Gong et al., 2020). The band gaps of MnO<sub>2</sub> and MnO<sub>2</sub>-40Fe are 2.15 eV and 1.55 eV, respectively (Fig. S8b). In order to further explore the characteristics of catalyst, the valence band spectra were measured for MnO<sub>2</sub> and MnO<sub>2</sub>-40Fe, as shown in Fig. S8c-d. The VB of MnO<sub>2</sub> and MnO<sub>2</sub>-40Fe are both 1 eV. The conduction band (CB) could be calculated by the following formula:  $E_{CB} = E_{VB} - E_g$ . The conduction bands are -1.15 eV and -0.55 eV for MnO<sub>2</sub> and MnO<sub>2</sub>-40Fe, respectively.

### 3.5. Degradation mechanism of MnO<sub>2</sub>-40Fe in photo-Fenton system

Importantly, MnO<sub>2</sub>-40Fe has the advantages of higher redox capacity and faster electron transfer rate than MnO<sub>2</sub>. Therefore, it can be inferred that loading nano zero-valent iron improves the performance of MnO<sub>2</sub> as an activator of H<sub>2</sub>O<sub>2</sub>. We also studied the effects of the different quenchers on degrading sulfadiazine by the photo-Fenton system, as shown in Fig. 4a. In general, \*OH is the primary radical in the photo-Fenton degradation process. Tertbutyl alcohol (TBA) is an effective quencher, inhibits the formation of \*OH on the catalyst surface (\*OH<sub>ads</sub>) and in the solution (\*OH<sub>free</sub>) (Yang et al., 2019). Adding 5 mM TBA prevents the degradation of sulfadiazine during the photo-Fenton reaction, the removal rate dropped to 23.8%, which was 0.24 times smaller than that with a no quencher.

In contrast, when same amounts of benzoquinone (BQ), AgNO<sub>3</sub> and EDTA added to suppress the production of \*O<sub>2</sub><sup>-</sup>, e<sup>-</sup> and h<sup>+</sup> in the system, it has a little effect on the degradation of sulfadiazine. Therefore, the role played by \*OH in the degradation of sulfadiazine is marked. The production of hydroxyl and superoxide free radicals in MnO<sub>2</sub>-40Fe/H<sub>2</sub>O<sub>2</sub>/light system was confirmed further by ESR spectroscopic data (Fig. 4b). In solution, the \*O<sub>2</sub><sup>-</sup> rapidly disproportionate into \*OH and HOO\*, and the lifetime of HOO\* is very short (He et al., 2020). It is worth noting that although \*O<sub>2</sub><sup>-</sup> and \*OH co-exist, the characteristic peak intensity of \*O<sub>2</sub><sup>-</sup> is not as apparent as \*OH. When compared to the data obtained in the MnO<sub>2</sub>/H<sub>2</sub>O<sub>2</sub>/light, the addition of DMPO- \*OH has 4 distinct peaks with an intensity ratio of 1:2:2:1 in the MnO<sub>2</sub>-40Fe/H<sub>2</sub>O<sub>2</sub>/light. Therefore, we can draw the conclusion that Fe(0) and light enhance the generation of hydroxyl radicals.

We also examined the concentration of iron species during the photo-Fenton degradation of sulfadiazine by MnO<sub>2</sub>-40Fe (Fig. S7f). The concentrations of Fe<sup>3+</sup> and Fe<sup>2+</sup> are similar before applying H<sub>2</sub>O<sub>2</sub> and light radiation. With the progress of the reaction, Fe<sup>3+</sup> concentration rises rapidly. At this time, the degradation rate of sulfadiazine was also the fastest during the entire reaction cycle. After 20 min, Fe<sup>2+</sup> concentration has decreased, which may lead to its rapid consumption by H<sub>2</sub>O<sub>2</sub> and the slow reduction of Fe<sup>3+</sup> to Fe<sup>2+</sup> (Dong et al., 2016). The total concentration of leached iron ions reaches 0.24 mg/L within 60 min. Compared with previous reports (Li et al., 2019; Li et al., 2020b), suggesting that iron leaching rate is low and the performance is stable for MnO<sub>2</sub>-40Fe. World Health Organization (WHO) requires that the total iron ion concentration should not exceed 0.3 mg/L in drinking water (Lyu et al., 2019). Obviously, the total iron ion dissolution of MnO<sub>2</sub>-40Fe is lower than the standard. MnO<sub>2</sub>-40Fe has no secondary pollution to the environment. Besides, the mass balance of iron ion in the solution does not vary significantly, which indicates that

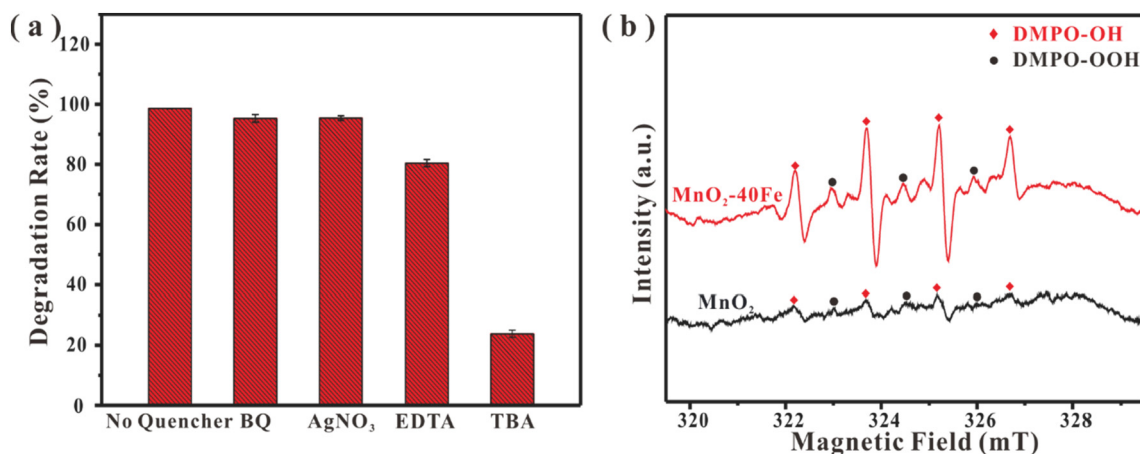


**Fig. 4.** The effect of quencher on degradation sulfadiazine (a) and ESR spectra of DMPO-<sup>\*</sup>OH adducts (b) for MnO<sub>2</sub> and MnO<sub>2</sub>-40Fe. (Experimental conditions: [SDZ]<sub>0</sub> = 20 mg/L, [H<sub>2</sub>O<sub>2</sub>]<sub>0</sub> = 6 mM, [Catalyst]<sub>0</sub> = 0.2 g/L, [pH]<sub>0</sub> = 3, T = 20 °C and 500 W xenon lamp.)

minimal loss of aqueous iron species as precipitates. Thus, the high catalytic activity of MnO<sub>2</sub>-40Fe does not change with repeated use.

The photo-Fenton mechanism of sulfadiazine degradation by MnO<sub>2</sub>-40Fe is shown in Fig. 5. The possible degradation reactions are shown below:

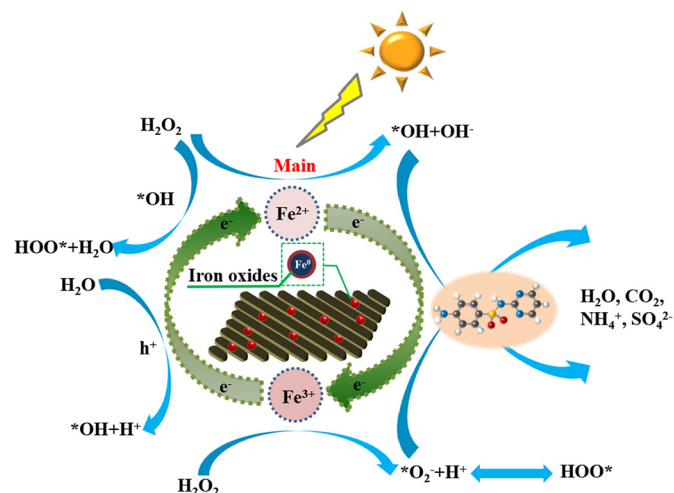
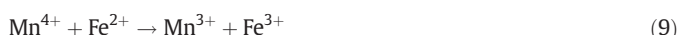
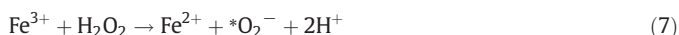
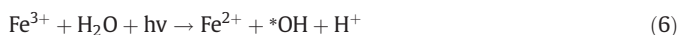


**Fig. 5.** Degradation mechanism of sulfadiazine in MnO<sub>2</sub>-40Fe/H<sub>2</sub>O<sub>2</sub>/light system.



There are some photo-Fenton degradation pathways during the reaction. In the dark, the degradation is not efficient due to the lack of photo-induced e<sup>-</sup> and h<sup>+</sup> (Eq. (2)) (Guo et al., 2019; Zhu et al., 2019). On the other hand, light can not only accelerate the formation of Fe<sup>2+</sup>, but also promote the reduction of Fe<sup>3+</sup> to Fe<sup>2+</sup> vis Eqs. (3) and (6) (Pan et al., 2019), thereby improving the reaction efficiency of the catalyst. Zero-valent iron, as the source of iron ions, is also the main mechanism of the photo-Fenton reaction at acidic conditions (Eq. (4)) (He et al., 2016). Both Fe<sup>2+</sup> and Fe<sup>3+</sup> react with H<sub>2</sub>O<sub>2</sub> to produce <sup>\*</sup>OH and <sup>\*</sup>O<sub>2</sub><sup>-</sup>, which makes sulfadiazine to be removed, as shown in Eqs. (5) and (7) (Yamaguchi et al., 2018; Yang et al., 2019). Photo-induced e<sup>-</sup> also promotes the cycle of Fe<sup>3+</sup> and Fe<sup>2+</sup> in Eq. (8) (Ji et al., 2020; Wang et al., 2016). It can be seen that Mn<sup>4+</sup> is reduced to Mn<sup>3+</sup>, undergoes a series of reactions similar to iron ions vis Eqs. (9)–(11) (Xu et al., 2019). In addition, the active substance produced by MnO<sub>2</sub> has a weak effect on sulfadiazine, which is consistent with the ESR spectrum. When bare MnO<sub>2</sub> was used in the presence of light, the holes produced tiny amounts of <sup>\*</sup>OH to degrade sulfadiazine (Habibi and Mosavi, 2017), as shown in Eqs. (2) and (12). It can be seen from Fig. 3a that the catalyst MnO<sub>2</sub> has low degradation efficiency. Eqs. (13) and (14) also play a role in the production of free radicals (Liu et al., 2018b; Mitchell et al., 2014), and the ERS data shown in Fig. 4b supports the notion. Indeed, all of these pathways co-exist and play synergistic roles for degradation of sulfadiazine by the photo-Fenton process. The presence of MnO<sub>2</sub> can be used not only as a catalyst of the photo-Fenton system, but also as the co-catalyst, and Fe(0) is the main body of Fenton system.

### 3.6. Degradation pathway of sulfadiazine in MnO<sub>2</sub>-40Fe/H<sub>2</sub>O<sub>2</sub>/light system

The reaction solution after photo-Fenton degradation was analyzed by LC-MS in the negative ion mode to study the degradation products of sulfadiazine, as shown in Fig. S9. Table S1 shows the intermediate products that result from photo-Fenton degradation for sulfadiazine, such as the measured [M-H]<sup>-</sup> m/z, the molecular formula of the structure.

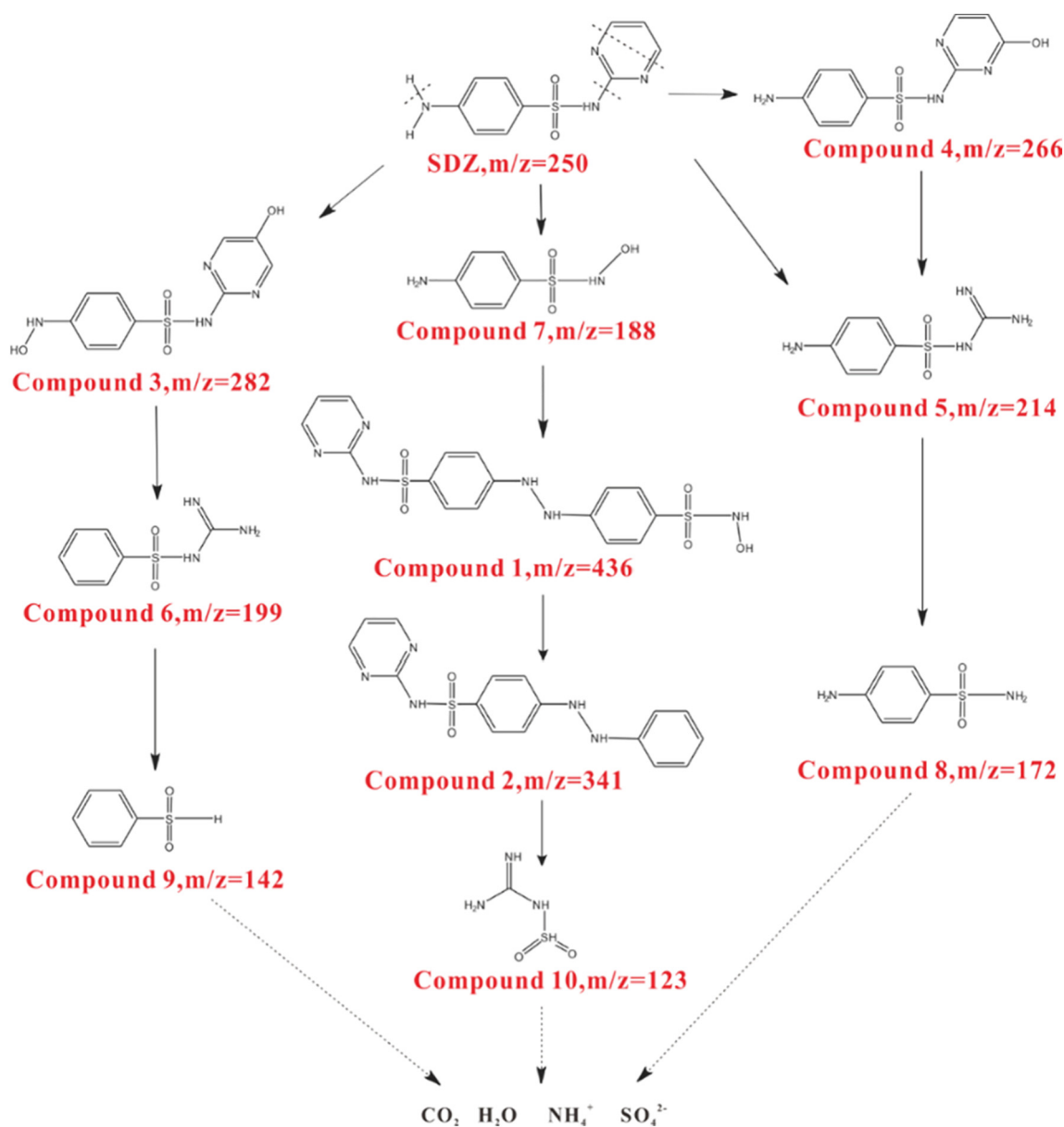


**Fig. 6.** Proposed degradation pathways of SDZ in the MnO<sub>2</sub>-40Fe/H<sub>2</sub>O<sub>2</sub>/light system. (Experimental conditions: [SDZ]<sub>0</sub> = 20 mg/L, [H<sub>2</sub>O<sub>2</sub>]<sub>0</sub> = 6 mM, [Catalyst]<sub>0</sub> = 0.2 g/L, [pH]<sub>0</sub> = 3, T = 20 °C and 500 W xenon lamp.)

Based on the known intermediates, as shown in Fig. 6, we infer four possible sulfadiazine degradation pathways. As reported elsewhere, hydroxyl radicals are very likely to attack H—N, N—C, S—N and N—C bonds in pyrimidine on sulfadiazine (Rong et al., 2014; Yang et al., 2014; Zhou et al., 2016). The results show that the first way to form compound 7 with m/z 188 is to break N—C bond of sulfadiazine. Sulfadiazine is prone to lose an electron at the N site, leading to the cleavage of the H—N bond to form sulfadiazine free radicals. These active free radicals undergo coupling reactions (Gao et al., 2012; Yang et al., 2017), and form compound 1 with m/z 436. The S—N bond of the dimer is attacked by <sup>\*</sup>OH to form compound 2 with m/z 341. Next, the second degradation pathway is that free radicals attack the H—N bond of sulfadiazine, and upon hydroxylation produces compound 3 with m/z 282. Under the continuous interactions with free radicals, compound 3 is likely to be transformed into compound 6 with m/z 199. Besides, compound 9 with m/z 142 can be formed by the cleavage of the N—S bond of compound 6. Sulfadiazine can also hydroxylate to produce compound 4 with m/z 266. Compound 5 with m/z 214 is

obtained by the cleavage of the C—N bond in the pyrimidine ring. The C—N bond on the benzene ring is further attacked by <sup>\*</sup>OH, resulting in compound 8 with m/z 172. The last degradation pathway is that the two N—C bonds on the pyrimidine are unstable and easily cleaved (Sun et al., 2018), directly forming compound 5. According to the reports, these compounds are further oxidized into small molecules (CO<sub>2</sub>, H<sub>2</sub>O) and inorganic ions (NH<sub>4</sub><sup>+</sup>, SO<sub>4</sub><sup>2-</sup>) by free radicals in the reaction system (Xu et al., 2020b; Zhou et al., 2016; Zhu et al., 2020).

### 3.7. Toxicity evaluation of sulfadiazine and its intermediates in MnO<sub>2</sub>-40Fe/H<sub>2</sub>O<sub>2</sub>/light system

There have been many studies on calculating of intermediates produced in the sulfadiazine degradation, but there are few studies on their potential toxicity risks. This should cause our attention. Therefore, we used T.E.S.T. to evaluate the mutagenicity and developmental toxicity of sulfadiazine and its degradation intermediates (Zhou et al., 2020), as shown in Fig. 7. Developmental toxicity refers to the extrapolated

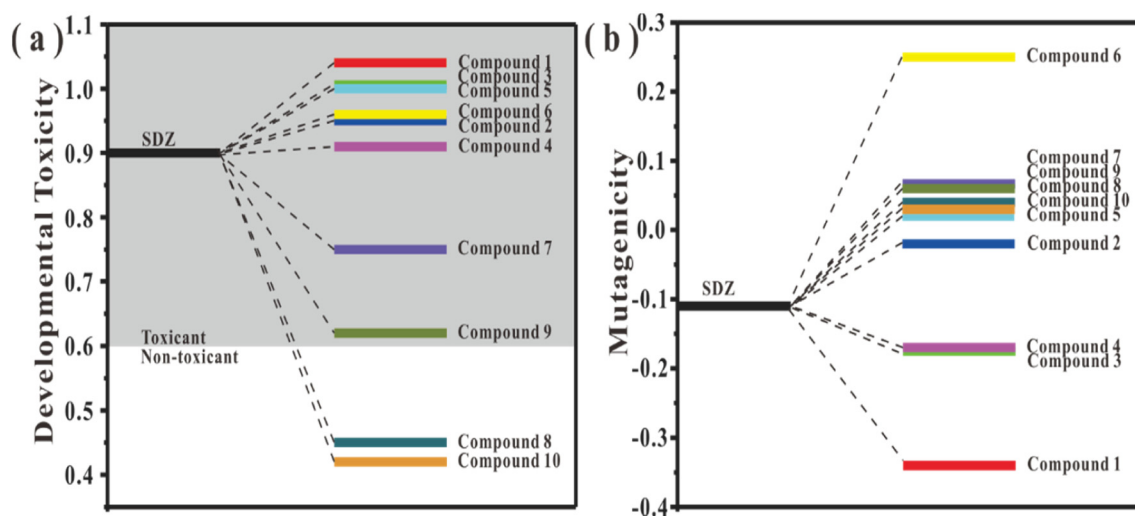


Fig. 7. Developmental toxicity (a) and mutagenicity (b) of sulfadiazine and its degradation intermediates in  $\text{MnO}_2\text{-40Fe}/\text{H}_2\text{O}_2/\text{light}$  system.

toxicity of chemical substances to humans and animals, which includes any effects that interfere with normal development before and after birth. The results suggest that the developmental toxicity of compounds 7–10 is lower than sulfadiazine, and compounds 8 and 10 are non-toxic. The coefficient 0.5 is the threshold value between negative and positive mutagenicity (Lu et al., 2020). Therefore, sulfadiazine and its intermediates are classified as mutagenicity negative. The final products of sulfadiazine are less threatening to the environment in  $\text{MnO}_2\text{-40Fe}/\text{H}_2\text{O}_2/\text{light}$  system.

### 3.8. Application and the stability of the $\text{MnO}_2\text{-40Fe}$

Catalysts were also prepared using the cathode materials of spent Li-ion batteries by the same method used for  $\text{MnO}_2\text{-40Fe}$  fabrication. The  $\text{MnO}_2\text{-40Fe}$  of the spent Li-ion batteries (after 100 times charging and discharging circulation, hereafter S- $\text{MnO}_2\text{-40Fe}$ ) was used to examine sulfadiazine degradation using optimal conditions derived under Section 3.2. The kinetics plots of sulfadiazine degradation by  $\text{MnO}_2\text{-40Fe}$ , F- $\text{MnO}_2\text{-40Fe}$  (fresh Li-ion cathode), and S- $\text{MnO}_2\text{-40Fe}$  are shown in Fig. 8. In all cases, the degradation rate of sulfadiazine by  $\text{MnO}_2\text{-Fe}$  composites shows first-order kinetics. The S- $\text{MnO}_2\text{-40Fe}$  shows the highest degradation efficiency of sulfadiazine (e.g. 99.6%) with a rate constant of  $0.094 \text{ min}^{-1}$ . The enhanced catalytic activity of

S- $\text{MnO}_2\text{-40Fe}$  is ascribed to changes of oxidation state, phase transition and charge density of  $\text{MnO}_2$  during inter-phasing Li ions with the  $\text{MnO}_2\text{-40Fe}$  at discharge stage (EunJoo Yoo et al., 2008).

The  $\text{MnO}_2\text{-40Fe}$  and S- $\text{MnO}_2\text{-40Fe}$  were used to determine the degradation efficiency of sulfadiazine after repeated use for five times, and the data are shown in Fig. 8b. When compared to  $\text{MnO}_2\text{-40Fe}$ , the performance of S- $\text{MnO}_2\text{-40Fe}$  shows enhanced reactivity and stability for sulfadiazine degradation. The binder used in spent cathode materials seems retarding  $\text{MnO}_2$  dissolution by enhancing its catalytic efficiency (Wang et al., 2018b). The data show the potential use of spent Li-ion batteries for pollution control programs; the re-use of Li-ion batteries reduces the accumulation of solid wastes, and also mitigation of antibiotics pollution.

Furthermore, we compared  $\text{MnO}_2\text{-40Fe}$  with metal oxides or improved metal oxide catalysts on the degradation of sulfadiazine that had been reported in the literature, as shown in Table 1. It clearly indicates that  $\text{MnO}_2\text{-40Fe}$  synthesized in this study has an excellent catalytic performance.

## 4. Conclusions

We fabricated a new catalyst using  $\text{MnO}_2$  and nano zero-valent iron composite by a hydrothermal method. The catalyst has a rod-like

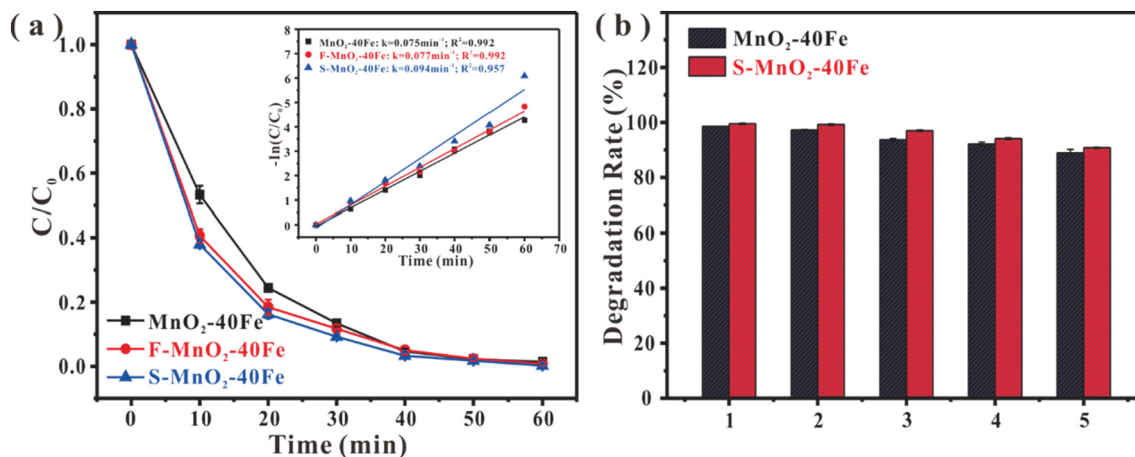


Fig. 8. Degradation effect, first-order kinetics (a) and five consecutive runs (b) of  $\text{MnO}_2\text{-40Fe}$ , S- $\text{MnO}_2\text{-40Fe}$  and F- $\text{MnO}_2\text{-40Fe}$ . (Experimental conditions:  $[\text{SDZ}]_0 = 20 \text{ mg/L}$ ,  $[\text{H}_2\text{O}_2]_0 = 6 \text{ mM}$ ,  $[\text{Catalyst}]_0 = 0.2 \text{ g/L}$ ,  $[\text{pH}]_0 = 3$ ,  $T = 20 \text{ }^\circ\text{C}$  and 500 W xenon lamp.)

**Table 1**  
Comparison of literature reports on the degradation of sulfadiazine.

Material	SDZ	Catalyst	H <sub>2</sub> O <sub>2</sub>	Reaction time	Efficiency	Ref.
AgBr/Ag <sub>3</sub> PO <sub>4</sub> /hematite	100 mg/L	0.17 g/L	–	300 min	95.8%	(Chen et al., 2019b)
TiO <sub>2</sub>	25 mg/L	2.5 g/L	–	90 min	89%	(Xu et al., 2020a)
TiO <sub>2</sub> /Fe	2.5 mg/L	0.5 g/L	–	60 min	~100%	(Baran et al., 2009)
g-C <sub>3</sub> N <sub>4</sub> nanosheets	20 mg/L	0.02 g/L	–	90 min	86%	(Liu et al., 2020)
Fe <sup>0</sup> /UV	0.4 mg/L	0.02 g/L	0.3 mM	60 min	98.8%	(Pan et al., 2019)
Siderite	10 mg/L	6 g/L	100 mM	90 min	98%	(Sun et al., 2020)
MnO <sub>2</sub> -40Fe	20 mg/L	0.2 g/L	6 mM	60 min	98.6%	This work

morphology, and the amount of iron leached from the material is negligible. Taking five experimental parameters as the research points, the sulfadiazine degradation efficiency of MnO<sub>2</sub>-40Fe was studied. The degradation rate of sulfadiazine can reach 98.6% by a heterogeneous photo-Fenton process. \*OH generated on the surface of MnO<sub>2</sub>-40Fe play a major role in MnO<sub>2</sub>-40Fe/H<sub>2</sub>O<sub>2</sub>/light system. In addition, MnO<sub>2</sub>-40Fe also has the good reusability. The same approach is used to fabricate MnO<sub>2</sub>-40Fe using the cathode materials of spent Li-ion batteries. This work provides a new way of reducing solid wastes generated by Li-ion batteries while protecting the aquatic systems against the pollution from antibiotics.

### CRedit authorship contribution statement

**Xing Chen:** Conceptualization, Supervision, Methodology, Writing – review & editing, Funding acquisition. **Fang Deng:** Methodology, Formal analysis, Investigation, Writing – original draft. **Xu Liu:** Investigation, Formal analysis. **Kang-Ping Cui:** Investigation, Formal analysis. **Rohan Weerasooriya:** Writing – review & editing.

### Declaration of competing interest

The authors declare that they have no known competing financial interests or personal relationships that could have appeared to influence the work reported in this paper.

### Acknowledgement

The authors acknowledge the financial support from the National Key R&D Program of China (2019YFC0408500), National Natural Science Foundation of China (Grant No. 21777164), Key Science and Technology Projects of Anhui Province (202003a07020004, and 201903a07020009), and Suzhou Science and Technology Plan Project (2019056). R. W. acknowledges the Program of Distinguished Professor in B&R Countries (Grant No. DL20180052).

### Appendix A. Supplementary data

Supplementary data to this article can be found online at <https://doi.org/10.1016/j.scitotenv.2021.145776>.

### References

- Bai, J., Liu, Y., Yin, X., Duan, H., Ma, J., 2017. Efficient removal of nitrobenzene by Fenton-like process with Co-Fe layered double hydroxide. *Appl. Surf. Sci.* 416, 45–50. <https://doi.org/10.1016/j.apsusc.2017.04.117>.
- Baquero, F., Martinez, J.L., Canton, R., 2008. Antibiotics and antibiotic resistance in water environments. *Curr. Opin. Biotechnol.* 19, 260–265. <https://doi.org/10.1016/j.copbio.2008.05.006>.
- Baran, W., Adamek, E., Sobczak, A., Makowski, A., 2009. Photocatalytic degradation of sulfa drugs with TiO<sub>2</sub>, Fe salts and TiO<sub>2</sub>/FeCl<sub>3</sub> in aquatic environment—kinetics and degradation pathway. *Appl. Catal., B* 90, 516–525. <https://doi.org/10.1016/j.apcatb.2009.04.014>.
- Barik, S.P., Prabakaran, G., Kumar, L., 2017. Leaching and separation of Co and Mn from electrode materials of spent lithium-ion batteries using hydrochloric acid: laboratory

- and pilot scale study. *J. Clean. Prod.* 147, 37–43. <https://doi.org/10.1016/j.jclepro.2017.01.095>.
- Chang, H., Hu, J., Wang, L., Shao, B., 2008. Occurrence of sulfonamide antibiotics in sewage treatment plants. *Chin. Sci. Bull.* 53, 514–520. <https://doi.org/10.1007/s11434-008-0123-x>.
- Chen, L., Jia, J., Ran, R., Song, X., 2019a. Nickel doping MnO<sub>2</sub> with abundant surface pits as highly efficient catalysts for propane deep oxidation. *Chem. Eng. J.* 369, 1129–1137. <https://doi.org/10.1016/j.cej.2019.03.142>.
- Chen, L., Yang, S., Huang, Y., Zhang, B., Kang, F., Ding, D., Cai, T., 2019b. Degradation of antibiotics in multi-component systems with novel ternary AgBr/Ag<sub>3</sub>PO<sub>4</sub>@natural hematite heterojunction photocatalyst under simulated solar light. *J. Hazard. Mater.* 371, 566–575. <https://doi.org/10.1016/j.jhazmat.2019.03.038>.
- Dickinson, M., Scott, T.B., 2010. The application of zero-valent iron nanoparticles for the remediation of a uranium-contaminated waste effluent. *J. Hazard. Mater.* 178, 171–179. <https://doi.org/10.1016/j.jhazmat.2010.01.060>.
- Dong, H., Sans, C., Li, W., Qiang, Z., 2016. Promoted discoloration of methyl orange in H<sub>2</sub>O<sub>2</sub>/Fe(III) Fenton system: effects of gallic acid on iron cycling. *Sep. Purif. Technol.* 171, 144–150. <https://doi.org/10.1016/j.seppur.2016.07.033>.
- Gao, J., Hedman, C., Liu, C., Guo, T., Pedersen, J.A., 2012. Transformation of sulfamethazine by manganese oxide in aqueous solution. *Environ. Sci. Technol.* 46, 2642–2651. <https://doi.org/10.1021/es202492h>.
- Gao, W., Zhang, X., Zheng, X., Lin, X., Cao, H., Zhang, Y., Sun, Z., 2017. Lithium carbonate recovery from cathode scrap of spent Lithium-ion battery: a closed-loop process. *Environ. Sci. Technol.* 51, 1662–1669. <https://doi.org/10.1021/acs.est.6b03320>.
- Gheju, M., Balcu, I., 2019. Sustaining the efficiency of the Fe(0)/H<sub>2</sub>O system for Cr(VI) removal by MnO<sub>2</sub> amendment. *Chemosphere* 214, 389–398. <https://doi.org/10.1016/j.chemosphere.2018.09.129>.
- Gomes, J., Costa, R., Quinta-Ferreira, R.M., Martins, R.C., 2017. Application of ozonation for pharmaceuticals and personal care products removal from water. *Sci. Total Environ.* 586, 265–283. <https://doi.org/10.1016/j.scitotenv.2017.01.216>.
- Gong, J., Li, Y., Zhao, Y., Wu, X., Zhang, G., 2020. Metal-free polymeric (SCN)<sub>n</sub> photocatalyst with adjustable bandgap for efficient organic pollutants degradation and Cr(VI) reduction under visible-light irradiation. *Chem. Eng. J.* 402, 126147. <https://doi.org/10.1016/j.cej.2020.126147>.
- Guo, T., Wang, K., Zhang, G., Wu, X., 2019. A novel α-Fe<sub>2</sub>O<sub>3</sub>@g-C<sub>3</sub>N<sub>4</sub> catalyst: synthesis derived from Fe-based MOF and its superior photo-Fenton performance. *Appl. Surf. Sci.* 469, 331–339. <https://doi.org/10.1016/j.apsusc.2018.10.183>.
- Habibi, M.H., Mosavi, V., 2017. Photo-catalytic activity of highly efficient binary Mn-Fe nano composite oxides for degradation of cresol fast violet: phase formation and band gap study. *J. Mater. Sci.-Mater. Electron.* 28, 13643–13648. <https://doi.org/10.1007/s10854-017-7206-x>.
- Hadi, S., Hajar, H.H., 2021. In situ synthesis of visible-light-driven α-MnO<sub>2</sub> nanorod/AgBr nanocomposites for increased photoinduced charge separation and enhanced photocatalytic activity. *Mater. Res. Bull.* 133, 111046. <https://doi.org/10.1016/j.materresbull.2020.111046>.
- Hao, S.J., Zhang, B.W., Feng, J.Y., Liu, Y.Y., Ball, S., Pan, J.S., Srinivasan, M., Huang, Y.Z., 2017. Nanoscale ion intermixing induced activation of Fe<sub>2</sub>O<sub>3</sub>/MnO<sub>2</sub> composites for application in lithium ion batteries. *J. Mater. Chem. A* 5, 8510–8518. <https://doi.org/10.1039/c7ta00172j>.
- Harper, G., Sommerville, R., Kendrick, E., Driscoll, L., Slater, P., Stolkin, R., Walton, A., Christensen, P., Heidrich, O., Lambert, S., Abbott, A., Ryder, K., Gaines, L., Anderson, P., 2019. Recycling lithium-ion batteries from electric vehicles. *Nature* 575, 75–86. <https://doi.org/10.1038/s41586-019-1682-5>.
- He, J., Yang, X., Men, B., Wang, D., 2016. Interfacial mechanisms of heterogeneous Fenton reactions catalyzed by iron-based materials: a review. *J. Environ. Sci.* 39, 97–109. <https://doi.org/10.1016/j.jes.2015.12.003>.
- He, X., Sun, B., He, M., Chi, H., Wang, Z., Zhang, W., Ma, J., 2020. Highly efficient simultaneous catalytic degradation and defluorination of perfluorooctanoic acid by the H<sub>2</sub>O<sub>2</sub>-carbon/MnO<sub>2</sub> system generating O<sub>2</sub>- and OH synchronously. *Appl. Catal., B* 277, 119219. doi:10.1016/j.apcatb.2020.119219.
- Ji, J., Yan, Q., Yin, P., Mine, S., Matsuoka, M., Xing, M., 2020. Tuning redox reactions via defects on CoS<sub>2-x</sub> for sustainable degradation of organic pollutants. *Angew. Chem. Int. Edit.* 59, 1–7. <https://doi.org/10.1002/anie.202013015>.
- Kennedy, R., F. Joel, A.P., 2006. Kinetics of oxytetracycline reaction with a hydrous manganese oxide. *Environ. Sci. Technol.* 40, 7216–7221. <https://doi.org/10.1021/es060357o>.
- Kümmerer, K., 2004. Resistance in the environment. *J. Antimicrob. Chemother.* 54, 311–320. <https://doi.org/10.1093/jac/dkh325>.

- Li, J., Xiao, C., Wang, K., Li, Y., Zhang, G., 2019. Enhanced generation of reactive oxygen species under visible light irradiation by adjusting the exposed facet of FeWO<sub>4</sub> nano-sheets to activate oxalic acid for organic pollutant removal and Cr(VI) reduction. *Environ. Sci. Technol.* 53, 11023–11030. <https://doi.org/10.1021/acs.est.9b00641>.
- Li, J., Zhang, X., Wang, T., Zhao, Y., Song, T., Zhang, L., Cheng, X., 2020a. Construction of layered hollow Fe<sub>3</sub>O<sub>4</sub>/Fe<sub>1-x</sub>S@MoS<sub>2</sub> composite with enhanced photo-Fenton and adsorption performance. *J. Environ. Chem. Eng.* 8, 103762. <https://doi.org/10.1016/j.jece.2020.103762>.
- Li, X., Cui, K., Guo, Z., Yang, T., Cao, Y., Xiang, Y., Chen, H., Xi, M., 2020b. Heterogeneous Fenton-like degradation of tetracyclines using porous magnetic chitosan microspheres as an efficient catalyst compared with two preparation methods. *Chem. Eng. J.* 379, 122324. <https://doi.org/10.1016/j.cej.2019.122324>.
- Lin, J., Liu, C., Cao, H., Chen, R., Yang, Y., Li, L., Sun, Z., 2019. Environmentally benign process for selective recovery of valuable metals from spent lithium-ion batteries by using conventional sulfation roasting. *Green Chem.* 21. <https://doi.org/10.1039/C9GC01350D>.
- Liu, X., Cao, Z., Yuan, Z., Zhang, J., Guo, X., Yang, Y., He, F., Zhao, Y., Xu, J., 2018a. Insight into the kinetics and mechanism of removal of aqueous chlorinated nitroaromatic antibiotic chloramphenicol by nanoscale zero-valent iron. *Chem. Eng. J.* 334, 508–518. <https://doi.org/10.1016/j.cej.2017.10.060>.
- Liu, X., Zhou, Y., Zhang, J., Luo, L., Yang, Y., Huang, H., Peng, H., Tang, L., Mu, Y., 2018b. Insight into electro-Fenton and photo-Fenton for the degradation of antibiotics: mechanism study and research gaps. *Chem. Eng. J.* 347, 379–397. <https://doi.org/10.1016/j.cej.2018.04.142>.
- Liu, Y., Fan, Q., Wang, J., 2018c. Zn-Fe-CNTs catalytic in situ generation of H<sub>2</sub>O<sub>2</sub> for Fenton-like degradation of sulfamethoxazole. *J. Hazard. Mater.* 342, 166–176. <https://doi.org/10.1016/j.jhazmat.2017.08.016>.
- Liu, Z.G., Zhang, X., Jiang, Z.X., Chen, H.S., Yang, P., 2019. Phosphorus and sulphur co-doping of g-C<sub>3</sub>N<sub>4</sub> nanotubes with tunable architectures for superior photocatalytic H<sub>2</sub> evolution. *Int. J. Hydrogen Energy* 44, 20042–20055. <https://doi.org/10.1016/j.ijhydene.2019.06.037>.
- Liu, M., Zhang, D., Han, J., Liu, C., Ding, Y., Wang, Z., Wang, A., 2020. Adsorption enhanced photocatalytic degradation sulfadiazine antibiotic using porous carbon nitride nano-sheets with carbon vacancies. *Chem. Eng. J.* 382, 123017. <https://doi.org/10.1016/j.cej.2019.123017>.
- Lu, J., Wang, T., Zhou, Y., Cui, C., Ao, Z., Zhou, Y., 2020. Dramatic enhancement effects of l-cysteine on the degradation of sulfadiazine in Fe<sup>3+</sup>/CaO<sub>2</sub> system. *J. Hazard. Mater.* 383, 121133. <https://doi.org/10.1016/j.jhazmat.2019.121133>.
- Lu, C., He, D., Mou, Z., Yang, X., 2019. Synergetic activation of peroxyoxysulfate by MnO<sub>2</sub>-loaded β-FeOOH catalyst for enhanced degradation of organic pollutant in water. *Sci. Total Environ.* 693, 133589. <https://doi.org/10.1016/j.scitotenv.2019.133589>.
- Michael, I., Rizzo, L., McArdell, C.S., Manai, C.M., Merlin, C., Schwartz, T., Dagot, C., Fatta-Kassinos, D., 2013. Urban wastewater treatment plants as hotspots for the release of antibiotics in the environment: a review. *Water Res.* 47, 957–995. <https://doi.org/10.1016/j.watres.2012.11.027>.
- Mitchell, S.M., Ahmad, M., Teel, A.L., Watts, R.J., 2014. Degradation of perfluorooctanoic acid by reactive species generated through catalyzed H<sub>2</sub>O<sub>2</sub> propagation reactions. *Environ. Sci. Technol. Lett.* 1, 117–121. <https://doi.org/10.1021/ez4000862>.
- Neafsey, K., Zeng, X., Lemley, A.T., 2010. Degradation of sulfonamides in aqueous solution by membrane anodic Fenton treatment. *J. Agric. Food Chem.* 58, 1068–1076. <https://doi.org/10.1021/jf904066a>.
- Pan, Y., Zhang, Y., Zhou, M., Cai, J., Tian, Y., 2019. Enhanced removal of antibiotics from secondary wastewater effluents by novel UV/pre-magnetized Fe<sup>0</sup>/H<sub>2</sub>O<sub>2</sub> process. *Water Res.* 153, 144–159. <https://doi.org/10.1016/j.watres.2018.12.063>.
- Patel, M., Kumar, R., Kishor, K., Misra, T., Pittman, C., Mohan, D., 2019. Pharmaceuticals of emerging concern in aquatic systems: chemistry, occurrence, effects, and removal methods. *Chem. Rev.* 119, 3510–3673. <https://doi.org/10.1021/acs.chemrev.8b00299>.
- Pignatello, J.J., Oliveros, E., Mackay, A., 2006. Advanced oxidation processes for organic contaminant destruction based on the Fenton reaction and related chemistry. *Crit. Rev. Environ. Sci. Technol.* 36, 1–84. <https://doi.org/10.1080/10643380500326564>.
- Ploychompoo, S., Chen, J., Luo, H., Liang, Q., 2020. Fast and efficient aqueous arsenic removal by functionalized MIL-100(Fe)/rGO/δ-MnO<sub>2</sub> ternary composites: adsorption performance and mechanism. *J. Environ. Sci.* 91, 24–36. <https://doi.org/10.1016/j.jes.2019.12.014>.
- Qu, Q., Fu, L., Zhan, X., Samuelis, D., Maier, J., Li, L., Tian, S., Li, Z.H., Wu, Y., 2011. Porous LiMn<sub>2</sub>O<sub>4</sub> as cathode material with high power and excellent cycling for aqueous rechargeable lithium batteries. *Energy Environ. Sci.* 4, 3985–3990. <https://doi.org/10.1039/C0EE00673D>.
- Rong, S.P., Sun, Y.B., Zhao, Z.H., 2014. Degradation of sulfadiazine antibiotics by water falling film dielectric barrier discharge. *Chin. Chem. Lett.* 25, 187–192. <https://doi.org/10.1016/j.ccl.2013.11.003>.
- Ruiz-Camacho, B., Baltazar Vera, J.C., Medina-Ramírez, A., Fuentes-Ramírez, R., Carreño-Aguilera, G., 2017. EIS analysis of oxygen reduction reaction of Pt supported on different substrates. *Int. J. Hydrogen Energy* 42, 30364–30373. <https://doi.org/10.1016/j.ijhydene.2017.08.087>.
- Sellers, R.M., 1980. Spectrophotometric determination of hydrogen peroxide using potassium titanium(IV) oxalate. *Analyst* 105, 950–954. <https://doi.org/10.1039/an9800500950>.
- Singh, R.K., Devivaraprasad, R., Kar, T., Chakraborty, A., Neergat, M., 2015. Electrochemical impedance spectroscopy of oxygen reduction reaction (ORR) in a rotating disk electrode configuration: effect of ionomer content and carbon-support. *J. Electrochem. Soc.* 162, 489–498. <https://doi.org/10.1149/2.0141506jes>.
- Song, X., Shi, Q., Wang, H., Liu, S., Tai, C., Bian, Z., 2017. Preparation of Pd-Fe/graphene catalysts by photocatalytic reduction with enhanced electrochemical oxidation-reduction properties for chlorophenols. *Appl. Catal., B* 203, 442–451. <https://doi.org/10.1016/j.apcatb.2016.10.036>.
- Sun, J., Wang, Q., Zhang, J., Wang, Z., Wu, Z., 2018. Degradation of sulfadiazine in drinking water by a cathodic electrochemical membrane filtration process. *Electrochim. Acta* 277, 77–87. <https://doi.org/10.1016/j.electacta.2018.05.005>.
- Sun, F., Liu, H., Wang, H., Shu, D., Chen, T., Zou, X., Huang, F., Chen, D., 2020. A novel discovery of a heterogeneous Fenton-like system based on natural siderite: a wide range of pH values from 3 to 9. *Sci. Total Environ.* 698, 134293. <https://doi.org/10.1016/j.scitotenv.2019.134293>.
- Tang, J., Wang, J., 2018. Metal organic framework with coordinatively unsaturated sites as efficient Fenton-like catalyst for enhanced degradation of sulfamethazine. *Environ. Sci. Technol.* 52, 5367–5377. <https://doi.org/10.1021/acs.est.8b00092>.
- Thiele-Bruhn, S., Aust, M.O., 2004. Effects of pig slurry on the sorption of sulfonamide antibiotics in soil. *Arch. Environ. Contam. Toxicol.* 47, 31–39. <https://doi.org/10.1007/s00244-003-3120-8>.
- To, T.B., Nordstrom, D.K., M.Cunningham, K., Ball, J.W., Mcleskey, R.B., 1999. New method for the direct determination of dissolved Fe(III) concentration in acid mine waters. *Environ. Sci. Technol.* 33, 807–813. <https://doi.org/10.1021/es980684z>.
- Wang, R.C., Lin, Y.C., Wu, S.H., 2009. A novel recovery process of metal values from the cathode active materials of the lithium-ion secondary batteries. *Hydrometallurgy* 99, 194–201. <https://doi.org/10.1016/j.hydromet.2009.08.005>.
- Wang, N., Zheng, T., Zhang, G., Wang, P., 2016. A review on Fenton-like processes for organic wastewater treatment. *J. Environ. Chem. Eng.* 4, 762–787. <https://doi.org/10.1016/j.jece.2015.12.016>.
- Wang, X.Y., Wang, A.Q., Ma, J., 2017. Visible-light-driven photocatalytic removal of antibiotics by newly designed C<sub>3</sub>N<sub>4</sub>/MnFe<sub>2</sub>O<sub>4</sub>-graphene nanocomposites. *J. Hazard. Mater.* 336, 81–92. <https://doi.org/10.1016/j.jhazmat.2017.04.012>.
- Wang, D.X., Wang, Y., Li, Q.Y., Guo, W.B., Zhang, F.C., Niu, S.S., 2018a. Urchin-like α-Fe<sub>2</sub>O<sub>3</sub>/MnO<sub>2</sub> hierarchical hollow composite microspheres as lithium-ion battery anodes. *J. Power Sources* 393, 186–192. <https://doi.org/10.1016/j.jpowsour.2018.05.017>.
- Wang, X., Qiu, H., Liu, H., Shi, P., Fan, J., Min, Y., Xu, Q., 2018b. Recycling application of waste Li-MnO<sub>2</sub> batteries as efficient catalysts based on electrochemical lithiation improve catalytic activity. *Green Chem.* 20, 4901–4910. <https://doi.org/10.1039/c8gc02183j>.
- Xiang, H., Guo, Y., Zhang, Z., Wang, H., Dong, S., Cheng, Y., 2019. Fabrication of MnO<sub>2</sub>/Fe rod-like composite with controllable weight ratios of Fe/MnO<sub>2</sub> and excellent wide-band electromagnetic absorption performance. *J. Alloys Compd.* 773, 150–157. <https://doi.org/10.1016/j.jallcom.2018.09.138>.
- Xu, L., Wang, J., 2011. A heterogeneous Fenton-like system with nanoparticulate zero-valent iron for removal of 4-chloro-3-methyl phenol. *J. Hazard. Mater.* 186, 256–264. <https://doi.org/10.1016/j.jhazmat.2010.10.116>.
- Xu, L., Wang, J., 2017. Magnetic nanoscale Fe<sub>3</sub>O<sub>4</sub>/CeO<sub>2</sub> composite as an efficient Fenton-like heterogeneous catalyst for degradation of 4-chlorophenol. *Environ. Sci. Technol.* 46, 10145–10153. <https://doi.org/10.1021/acs.est.7b0303f>.
- Xu, N., Guo, D., Xiao, C., 2019. Fe/Mn oxide decorated polyacrylonitrile hollow fiber membrane as heterogeneous Fenton reactor for methylene blue decolorization. *J. Appl. Polym. Sci.* 136, 48217. <https://doi.org/10.1002/app.48217>.
- Xu, L., Zhang, X., Han, J., Gong, H., Gan, L., 2020a. Degradation of emerging contaminants by sono-Fenton process with in situ generated H<sub>2</sub>O<sub>2</sub> and the improvement by P25-mediated visible light irradiation. *J. Hazard. Mater.* 391, 122229. <https://doi.org/10.1016/j.jhazmat.2020.122229>.
- Xu, X., Meng, L., Dai, Y., Zhang, M., Sun, C., Yang, S., He, H., Wang, S., Li, H., 2020b. Bi-spheres SPR-coupled Cu<sub>2</sub>O/Bi<sub>2</sub>MoO<sub>6</sub> with hollow spheres forming Z-scheme Cu<sub>2</sub>O/Bi<sub>2</sub>MoO<sub>6</sub> heterostructure for simultaneous photocatalytic decontamination of sulfadiazine and Ni(II). *J. Hazard. Mater.* 381, 120953. <https://doi.org/10.1016/j.jhazmat.2019.120953>.
- Yamaguchi, R., Kurosu, S., Suzuki, M., Kawase, Y., 2018. Hydroxyl radical generation by zero-valent iron/Cu (ZVI/Cu) bimetallic catalyst in wastewater treatment: heterogeneous Fenton/Fenton-like reactions by Fenton reagents formed in-situ under oxic conditions. *Chem. Eng. J.* 334, 1537–1549. <https://doi.org/10.1016/j.cej.2017.10.154>.
- Yan, W.L., Herzin, A.A., Li, X.Q., Kiely, C.J., Zhang, W.X., 2010. Structural evolution of Pd-doped nanoscale zero-valent iron (nZVI) in aqueous media and implications for particle aging and reactivity. *Environ. Sci. Technol.* 44, 4288–4294. <https://doi.org/10.1021/es100051q>.
- Yang, J.F., Zhou, S.B., Xiao, A.C., Li, W.J., Ying, G.G., 2014. Chemical oxidation of sulfadiazine by the Fenton process: kinetics, pathways, toxicity evaluation. *J. Environ. Sci. Health Part B* 49, 909–916. <https://doi.org/10.1080/03601234.2014.951572>.
- Yang, Y., Huang, G., Xu, S., He, Y., Liu, X., 2016. Thermal treatment process for the recovery of valuable metals from spent lithium-ion batteries. *Hydrometallurgy* 165, 390–396. <https://doi.org/10.1016/j.hydromet.2015.09.025>.
- Yang, J.F., Yang, L.M., Ying, G.G., Liu, C.B., Zheng, L.Y., Luo, S.L., 2017. Reaction of antibiotic sulfadiazine with manganese dioxide in aqueous phase: kinetics, pathways and toxicity assessment. *J. Environ. Sci. Health Part A* 52, 135–143. <https://doi.org/10.1080/10934529.2016.1237138>.
- Yang, Y., Xu, L., Li, W., Fan, W., Song, S., Yang, J., 2019. Adsorption and degradation of sulfadiazine over nanoscale zero-valent iron encapsulated in three-dimensional graphene network through oxygen-driven heterogeneous Fenton-like reactions. *Appl. Catal., B* 259, 118057. <https://doi.org/10.1016/j.apcatb.2019.118057>.
- Yoo, E., Kim, J., Hosono, E., Zhou, H.S., Kudo, T., Honma, I., 2008. Large reversible Li storage of graphene nanosheet families for use in rechargeable lithium ion batteries. *Nano Lett.* 8, 2277–2282. <https://doi.org/10.1021/nl800957b>.
- Zhang, C.L., Wen, C.B., Wang, Y., Wang, F.A., 2007. Determination of sulfadiazine in soil by spectrophotometry. *J. Anal. Sci.* 23, 616–618. [https://doi.org/10.1016/S1872-2040\(07\)60090-5](https://doi.org/10.1016/S1872-2040(07)60090-5).
- Zhang, Y., Zhou, J., Chen, X., Wang, L., Cai, W., 2019. Coupling of heterogeneous advanced oxidation processes and photocatalysis in efficient degradation of tetracycline

- hydrochloride by Fe-based MOFs: synergistic effect and degradation pathway. *Chem. Eng. J.* 369, 745–757. <https://doi.org/10.1016/j.cej.2019.03.108>.
- Zhao, Z., Geng, C., Yang, C., Cui, F., Liang, Z., 2018. A novel flake-ball-like magnetic Fe<sub>3</sub>O<sub>4</sub>/γ-MnO<sub>2</sub> meso-porous nano-composite: adsorption of fluorinon and effect of water chemistry. *Chemosphere* 209, 173–181. <https://doi.org/10.1016/j.chemosphere.2018.06.104>.
- Zhou, T., Zou, X., Mao, J., Wu, X., 2016. Decomposition of sulfadiazine in a sonochemical Fe<sup>0</sup>-catalyzed persulfate system: parameters optimizing and interferences of wastewater matrix. *Appl. Catal. B Environ.* 185, 31–41. <https://doi.org/10.1016/j.apcatb.2015.12.004>.
- Zhou, Y., He, J., Lu, J., Liu, Y., Zhou, Y., 2020. Enhanced removal of bisphenol A by cyclodextrin in photocatalytic systems: degradation intermediates and toxicity evaluation. *Chin. Chem. Lett.* 31, 2623–2626. <https://doi.org/10.1016/j.ccl.2020.02.008>.
- Zhu, Y., Zhu, R., Xi, Y., Zhu, J., Zhu, G., He, H., 2019. Strategies for enhancing the heterogeneous Fenton catalytic reactivity: a review. *Appl. Catal., B* 255, 117739. <https://doi.org/10.1016/j.apcatb.2019.05.041>.
- Zhu, L., Ji, J., Liu, J., Mine, S., Matsuoka, M., Zhang, J., Xing, M., 2020. Designing 3D-MoS<sub>2</sub> sponge as excellent cocatalysts in advanced oxidation processes for pollutant control. *Angew. Chem. Int. Edit.* 59, 13968–13976. <https://doi.org/10.1002/anie.202006059>.